INTERNATIONAL JOURNAL FOR NUMERICAL METHODS IN FLUIDS
Int. J. Numer. Meth. Fluids 2002; **38**:43–69 (DOI: 10.1002/fld.203)

Suppression of vortex shedding for flow around a circular cylinder using optimal control

C. Homescu[1,2], I. M. Navon[1,2,*,†] and Z. Li[2]

[1] *Department of Mathematics, Florida State University, Tallahassee, FL 32306, U.S.A.*
[2] *School of Computational Science and Information Technology, Florida State University, Tallahassee, FL 32306, U.S.A.*

SUMMARY

Adjoint formulation is employed for the optimal control of flow around a rotating cylinder, governed by the unsteady Navier–Stokes equations. The main objective consists of suppressing Karman vortex shedding in the wake of the cylinder by controlling the angular velocity of the rotating body, which can be constant in time or time-dependent. Since the numerical control problem is ill-posed, regularization is employed. An empirical logarithmic law relating the regularization coefficient to the Reynolds number was derived for $60 \leqslant Re \leqslant 140$. Optimal values of the angular velocity of the cylinder are obtained for Reynolds numbers ranging from $Re = 60$ to $Re = 1000$. The results obtained by the computational optimal control method agree with previously obtained experimental and numerical observations. A significant reduction of the amplitude of the variation of the drag coefficient is obtained for the optimized values of the rotation rate. Copyright © 2002 John Wiley & Sons, Ltd.

KEY WORDS: adjoint method; optimal control; rotating cylinder; Navier–Stokes equations; regularization; vortex shedding

1. INTRODUCTION

The viscous flow past a circular cylinder has been extensively studied due to its simple geometry and its representative behavior of general bluff body wakes. A deep understanding of the control strategies necessary to control flows past rotating bluff bodies could be applied in areas like drag reduction, lift enhancement, noise and vibration control, aerodynamics, etc.

A very important characteristic of this flow is the Karman vortex shedding (which has been extensively studied for the last 90 years, starting with the pioneering work of von Karman [1]).

Research on the problem of a flow past a cylindrical rotating body has been the subject of many experimental [2–4], and numerical investigations [5–9]. However, most

* Correspondence to: Prof I. M. Navon, School of Computational Science and Information Technology, Florida State University, Tallahassee, FL 32306, U.S.A.
† E-mail: navon@csit.fsu.edu

Contract/grant sponsor: NSF; contract/grant number: ATM-9731472

Received 21 December 2000
Revised 29 March 2001

of these results are primarily focused on the study of formation and development of vortices in a cylinder wake and they do not attempt to suppress vortex shedding.

Examples of applying control of vortex shedding in experiments are given by Gad-el-Hak [10, 11] and Modi [12]. Modi's experiments are related to the moving surface boundary layer control for airfoils. The moving surfaces are provided by rotating cylinders located at the leading edge and/or trailing edge as well as at the top surface of an airfoil. It has been shown that this mechanism of moving surfaces can prevent flow separation by retarding the initial growth of the boundary layer, with important consequences for lift enhancement and stall delay. The control parameter used was the speed ratio (which represents the ratio of cylinder speed to the free stream speed). This speed ratio can be either constant in time or time-dependent (e.g. if the airfoil is undergoing a rapid maneuver). This type of result provided us with the motivation to consider flow control for either a constant or time-dependent angular rotation of the cylinder.

Different approaches for the control of a flow around a cylinder have been successfully employed in the last two decades. For example, Tang and Aubry [13] suppressed the vortex shedding by inserting two small vortex perturbations in the flow; Gillies [14] used neural networks; Gunzburger and Lee [15] determined the amount of fluid injected or sucked on the rear of the cylinder from a feedback law depending on pressure measurements at stations along the surface of the cylinder; Huang [16] suppressed vortex shedding by feedback sound; Joslin *et al.* [17] showed that flow instabilities can be controlled by wave cancellation; Kwon and Choi [18], Ozono [19] and You *et al.* [20] employed splitter plates attached to the cylinder; Park *et al.* [21] used a pair of blowing/suction slots located on the surface of the cylinder; Sakamoto and Haniu [22] introduced a smaller cylinder near the main cylinder, with experiments conducted by changing the gap between the cylinders and the angle along the circumference from the front stagnation point of main cylinder; the flow is controlled via cylinder rotation (see e.g. References [23–27]); Pentek and Kadtke [28] implemented a chaos control scheme to capture and stabilize a concentrated vortex around the cylinder, the control being actuated by uniformly rotating the cylinder and actively changing the background flow velocity far from the body.

Due to the complexity and large dimensions of the control problem suboptimal control strategies have been considered and implemented. The concept of *instantaneous control* (e.g. control at every time step of the underlying dynamical systems) was applied in Choi *et al.* [29]. Another approach involves two stages: *first the approximation of the equations of the fluid flow using reduced order models and then an exact optimization for the reduced system*, the difference among various research efforts consisting in the choice of the basis functions used for the reduced models. In the reduced basis approach one uses as basis functions the terms which arise in series expansion of the solution with respect to a parameter (e.g. Ito and Ravindran [30]). The proper orthogonal decomposition (POD) approach is applied by Graham *et al.* [31, 32] and Afanasiev and Hinze [33].

Optimal control methods (OCM) have been employed for flow control. *Distributed controls* were used by Abergel and Temam [34], Gunzburger *et al.* [35], Hou *et al.* [36, 37]; *blowing and suction* on the surface of the cylinder was studied by Berggren [38], Bewley *et al.* [38], Ghattas and Bark [40], Li *et al.* [41]; *velocity tracking* (boundary velocity controls) was employed by Gunzburger and Manservisi [42], Gunzburger *et al.* [43], Hou and Ravindran [44, 45].

A key component of the process of flow control is the minimization of a cost functional aiming at the optimization of some of the flow characteristics.

Abergel and Temam [34] minimized the turbulence for a flow respectively driven by volume forces, a gradient of temperature and a gradient of pressure (the turbulence being measured by a L^2 norm of the curl of v ($\|\nabla \times v\|_{L^2}$) or, respectively, by studying the stress at the boundary); Berggren [38] minimized the vorticity field. Bewley *et al.* [39] reduced the turbulent kinetic energy and drag; Ghattas and Bark [40] used as objective function the rate at which energy is dissipated in the fluid.

The present article presents the numerical solution to the problem of controlling vortex shedding for a flow past a rotating cylinder using full optimal control. It is shown that the nature of the vortex shedding process is significantly altered by cylinder rotation. In this article we use global control (the entire body is subjected to prescribed motion) compared to the approach of local control (e.g. blowing/suction as reported by Li *et al.* [41]).

The mathematical formulation of the problem implies minimization of a cost functional. Since all efficient local minimization algorithms require the computation of the gradient of an objective functional (which will be described in a later section) with respect to the control parameters, part of this effort was dedicated to the gradient computation.

The adjoint method was employed to obtain the gradient of the discrete cost functional. The adjoint was constructed directly from the source code of the original discrete nonlinear model, circumventing difficulties that would appear if one were to first obtain the continuous adjoint model and then discretize the adjoint equations (for more about the differences between the *differentiate-then-discretize* approach and the *discretize-then-differentiate* approach see Gunzburger [46]).

The objective functional includes a regularization term since the optimization problem is ill-posed. Another important characteristic is the length of the 'control' window (the time window employed for minimization). It was found that the length of this time window should be larger than the vortex shedding period if the angular velocity (which serves as the control parameter) is time-dependent. However, if the angular velocity is constant in time, the length of the time window should only exceed a certain threshold value which can be smaller than the vortex shedding period.

The results obtained show that vortex shedding is suppressed for regimes of flow for $60 \leqslant Re \leqslant 1000$. For the same values of optimal rotation rate employed to achieve the elimination of the vortex shedding, the time histories of the drag coefficient show that a significant reduction in the amplitude of its variation is obtained compared to the case of the fixed cylinder.

The article is organized as follows. Section 2 introduces the flow model and its discretization in space and time. The optimal control problem is stated in Section 3 which includes formulation, cost functional(s), control parameters, description of the minimization using a quasi-Newton-type method and the discussion of the regularization term. The adjoint method for the computation of the gradient of the cost functional with respect to the control parameters is presented in Section 4. Procedures for the validation of the adjoint code and for checking the accuracy of the gradient computed using the adjoint model are presented in Appendices A and B. Numerical results related to suppression of Karman vortex street and time-histories of the drag coefficient are presented in Section 5. This section also includes some discussion of physical phenomena related to the flow around a rotating circular cylinder. Finally, Section 6 presents the summary and conclusions.

2. THE GOVERNING EQUATIONS OF THE MODEL

Let B denote a circular cylinder enclosed by an impermeable boundary Γ, while the two-dimensional exterior domain $\mathbf{D} = \mathbf{R}^2 \backslash \{B \cup \Gamma\}$ is the region occupied by an incompressible viscous fluid (for numerical purposes, the domain will be restricted to a rectangle in $\mathbf{R}^2$).

The fluid is moving with velocity U_0 in the x-direction and the cylinder rotates counter-clockwise with angular velocity $\mathbf{\Omega}$.

The problem can be mathematically described by the 2-D unsteady Navier–Stokes equations, where (u, v) is the velocity vector and p is the pressure:

$$\frac{\partial u}{\partial t} + \frac{\partial p}{\partial t} = \frac{1}{Re}\left(\frac{\partial^2 u}{\partial x^2} + \frac{\partial^2 u}{\partial y^2}\right) - \frac{\partial (u^2)}{\partial x} - \frac{\partial (uv)}{\partial y} \quad \text{in } \mathbf{D} \tag{1}$$

$$\frac{\partial v}{\partial t} + \frac{\partial p}{\partial y} = \frac{1}{Re}\left(\frac{\partial^2 v}{\partial x^2} + \frac{\partial^2 v}{\partial y^2}\right) - \frac{\partial (uv)}{\partial x} - \frac{\partial (v^2)}{\partial y} \quad \text{in } \mathbf{D} \tag{2}$$

$$\frac{\partial u}{\partial x} + \frac{\partial v}{\partial y} = 0 \quad \text{in } \mathbf{D} \tag{3}$$

subject to initial condition

$$(u, v)|_{t=0} = (u_0, v_0) \quad \text{in } \mathbf{D} \tag{4}$$

The equations are non dimensional. Re is the Reynolds number defined as $Re = U_0 d/v$, where d is the diameter of the cylinder and v is the viscosity.

No-slip boundary conditions are enforced at the upper and lower boundaries; an inflow boundary condition is applied at the left boundary:

$$u = U_0 \quad \text{and} \quad v = 0 \tag{5}$$

and an outflow boundary condition at the right boundary:

$$\frac{\partial u}{\partial x} = 0 \quad \text{and} \quad \frac{\partial v}{\partial x} = 0 \tag{6}$$

On the surface of the cylinder the velocity is equal to the angular velocity $\mathbf{\Omega} = (\mathbf{\Omega}_x, \mathbf{\Omega}_y)$:

$$u = \mathbf{\Omega}_x \qquad v = \mathbf{\Omega}_y \tag{7}$$

2.1. Space and time discretization

The region $\mathbf{D}$ is discretized using a staggered grid in which the pressure p is located at the cell centers, the horizontal velocity u at the midpoints of the vertical cell edges and the vertical velocity v at the midpoints of the horizontal cell edges. A finite volume space discretization is employed throughout. We require that the discretized values of u and v on the boundary cells be equal to the components of the angular velocity on the circle. Since the vertical boundaries contain no v-values and the horizontal boundaries contain no u-values, this boundary condition is enforced by averaging the values on either side of the boundary and setting this average to be equal to the angular velocity value.

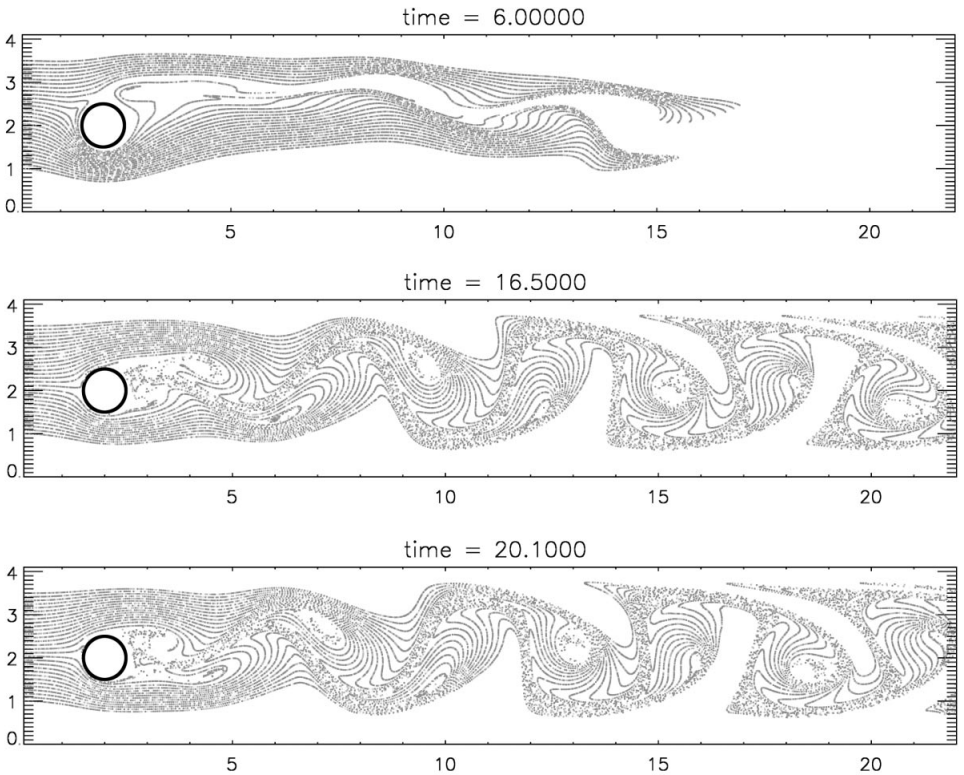

Figure 1. Streaklines for uncontrolled flow at $Re = 100$ and speed ratio $\alpha = 0.5$.

The time discretization is explicit in the velocities and implicit in the pressure: i.e. the velocity field at each time step t_{n+1} can be computed once the corresponding pressure was computed. The time step is required to satisfy the stability condition:

$$\delta t = \tau \min\left(\frac{Re}{2}\left(\frac{1}{\delta x^2} + \frac{1}{\delta y^2}\right)^{-1}, \frac{\delta x}{u_{\max}}, \frac{\delta y}{v_{\max}}\right)$$

where $\tau \in [0, 1]$ is the Courant–Fredrichs–Levy (CFL) number (set to 0.6 in the code).

More details about the time and space discretization may be found in Griebel *et al.* [47].

2.2. *Problem specification*

The domain is a rectangle of 22.0 units in length and 4.1 units in width. The cylinder (located inside the rectangle) measures 1.0 units in diameter and is situated at a distance of 1.5 units from the left boundary and 1.6 units from the upper boundary of the domain.

The cylinder is rotating with an angular velocity which can be either constant in time or a sinusoidal function.

Figure 1 shows the uncontrolled flow for this domain.

3. SOLVING THE OPTIMAL CONTROL PROBLEM

3.1. Formulation of the optimal control problem

The control problem consists in finding the optimal angular velocity of the cylinder such that the Karman vortex shedding in the wake of the cylinder is suppressed.

In order to find the optimal value(s) of the angular velocity of the cylinder, we minimize a cost functional which depends on the state variables as well as on the control variables (i.e. the rotation parameters: amplitude A and frequency F).

3.2. Possible cost functionals

Based on recent research work (e.g. References [34, 38–40, 48, 49]), several possible approaches to control the behavior of the flow can be employed, such as: *flow tracking* (the velocity field should be 'close' to a desired field); *enstrophy minimization* (the vorticity is minimized); *dissipation function* (minimize the rate at which heat is generated by deformations of the velocity field).

In this research work we considered only *flow tracking* and *vorticity minimization*. The mathematical expressions of the corresponding cost functionals are provided in the next subsection.

3.3. Mathematical formulation of the problem

If $\mathbf{\Lambda}$ *is the vector of parameters which determine the angular velocity of the cylinder, minimize the cost functional* J *with respect to* $\mathbf{\Lambda}$ *subject to the constraints imposed by the 2-D unsteady Navier–Stokes equations model.*

We considered a cost functional for vorticity minimization of the form:

$$J(\Lambda) = \frac{1}{2} \int_{t_1}^{t_2} \int_{\mathbf{D}} (\zeta^2) \, \mathrm{d}\mathbf{D} \, \mathrm{d}t \tag{8}$$

where the vorticity is $\zeta(x, y) = [(\partial u/\partial y)] - [(\partial v/\partial x)]$.

The best results were obtained when the cost functional J was chosen to be of the *flow tracking*-type, namely:

$$J(\Lambda) = \frac{1}{2} \int_{t_1}^{t_2} \int_{\mathbf{D}} (|u - u_d|^2 + |v - v_d|^2) \, \mathrm{d}\mathbf{D} \, \mathrm{d}t \tag{9}$$

where $\mathbf{D}$ is the spatial domain and (u_d, v_d) is the desired velocity field.

We will discuss in this paper only the results obtained for this objective functional since the best results were obtained for the cost functional of the flow-tracking type.

3.4. Description of the vector of control parameters $\mathbf{\Lambda}$

We define the speed ratio $\alpha \equiv a\Omega/U$, where a is the radius of the cylinder, Ω is the angular velocity and U is the free stream velocity.

We considered both the *constant rotation* case: $\alpha(t) = A$ as well as the *time harmonic rotary oscillation* case: $\alpha(t) = A \sin(2\pi F t)$.

The vector of control parameters is $\mathbf{\Lambda} = A$ or $\mathbf{\Lambda} = (A, F)$ respectively.

3.5. Existence of the optimal solution

The control problem involving Navier–Stokes equations was studied by Abergel and Temam [34], Coron [50], Fursikov *et al.* [51].

Ou [49] proved an existence theorem for the optimal controls in the case of a rotating cylinder, continuing the research of Sritharan [52].

3.6. Minimization

The algorithm used here for minimization for the objective function J is a quasi-Newton unconstrained minimization type method.

We started with the identity matrix and then iteratively, a better approximation $\mathbf{H}_i$ to the inverse Hessian matrix was built up, in such a way that the matrix $\mathbf{H}_i$ preserves positive definiteness and symmetry.

Using this approximation we constructed the new point:

$$\mathbf{x}_{i+1} = \mathbf{x}_i + \mathbf{H}_{i+1} \cdot (\nabla J(\mathbf{x}_{i+1}) - \nabla J(\mathbf{x}_i))$$

where the new approximation to the inverse Hessian $\mathbf{H}_{i+1}$ is constructed using the Davidon–Fletcher–Powell (DFP) rank-2 update formula.

We employed a modified version of the backtracking strategy implemented in Numerical Recipes [53] to choose a step along the direction of the Newton step $\mathbf{p}$. The goal was to move to a new point x_{new} along the direction of the Newton step $\mathbf{p}$:

$$\mathbf{x}_{\text{new}} = \mathbf{x}_{\text{old}} + \lambda \mathbf{p}, \quad 0 < \lambda \leqslant \lambda_0 \leqslant 1$$

such that the function

$$g(\lambda) = J(\mathbf{x}_{\text{old}} + \lambda \mathbf{p})$$

showed a sufficient decrease.

The convergence criteria used here are

$$J(\mathbf{x}_{\text{new}}) \leqslant J(\mathbf{x}_{\text{old}}) + \sigma \nabla J \cdot (\mathbf{x}_{\text{new}} - \mathbf{x}_{\text{old}}), \quad 0 < \sigma < 1$$

or $\|\nabla J(\mathbf{x}_{\text{new}})\| < 10^{-5}$.

3.7. Regularization

The numerical experiments proved that the minimization is ill-posed (e.g. while the objective functional decreased by a very small percentage, the difference in the values of the parameter for which we have this decrease in the function may assume *arbitrarily large values*).

Our approach for dealing with ill-posedness is to apply a Tikhonov-type regularization. We added a new term to the cost functional F:

$$F_{\text{REG}} = F + \lambda \Pi \tag{10}$$

where $\lambda > 0$ is a regularization parameter and Π a regularization function (see Tikhonov and Arsenin [54]).

The regularization term may also be viewed as playing the role of a penalty term aiming to ensure that the control parameter lies within a reasonable interval.

For the case of constant rotation the regularization function Π is:

$$\Pi = \frac{1}{2}\int_{\Gamma}(u^2+v^2)\,\mathrm{d}\Gamma$$

where (u,v) are the two components of velocity and Γ is the boundary of the cylinder.

Such a choice was also made by Abergel and Temam [34] and Gunzburger and Manservisi [42] in their research.

For the time-harmonic case, the regularization function Π is chosen to be:

$$\Pi = \int_0^{T_w}\frac{1}{2}\int_{\Gamma}(u^2+v^2)\,\mathrm{d}\Gamma$$

where T_w is the length of the time window for optimization.

For an in-depth discussion about different methods for solving ill-posed problems see Hansen [55] and Alifanov *et al.* [56].

4. THE ADJOINT METHOD

In this section we present the adjoint method for the computation of the gradient of the cost functional with respect to the control parameters.

The cost functional assumes the following form:

$$\mathbf{J}[X,\Lambda] = \frac{1}{2}\sum_{k=0}^{R}[\mathbf{X}(t_k)-\mathbf{X}^{\mathrm{obs}}(t_k)]^T\mathbf{W}(t_k)[\mathbf{X}(t_k)-\mathbf{X}^{\mathrm{obs}}(t_k)] \tag{11}$$

where $\mathbf{W}(t_k)$ is a diagonal weighting matrix, $t_0 \leqslant t_k \leqslant t_R$, $[t_0,t_R]$ the minimization window and R is the number of time steps in the minimization window.

To find the minimum of the cost functional, efficient minimization algorithms require the calculation of the gradient $(\nabla_\Lambda \mathbf{J}[\Lambda])^T$ of the cost functional with respect to the control parameters.

In Appendix A we provide a detailed description of the process of obtaining the gradient $(\nabla_\Lambda \mathbf{J}[\Lambda])^T$ using the adjoint variables $\hat{\mathbf{\Lambda}}$ satisfying the adjoint equations (which are also defined in Appendix A).

The gradient of the cost function with respect to the control parameters is:

$$\nabla_\Lambda \mathbf{J}[X] = \sum_{k=0}^{R}\hat{\mathbf{\Lambda}}^{(k)}(t_k)$$

$\nabla_\Lambda \mathbf{J}[X,\Lambda]$ can be obtained after the following algorithmic steps:

1. Integrate the adjoint model backwards from t_R to t_0 with zero final conditions for the adjoint variables.
2. The right-hand side in Equation (A8) (the forcing term) $\mathbf{W}(t_k)[\mathbf{X}(t_k)-\mathbf{X}^{\mathrm{obs}}(t_k)]$ is inserted whenever an analysis time t_k, $(k=1,\ldots,R)$ is reached.
3. At time $t=t_0$ the gradient of the cost functional with respect to the control variables is obtained.

The discrete operations in the forward model have unique corresponding discrete operations in the adjoint model. The derivation of the adjoint discrete model provides us with a method

to employ the original computer code (corresponding to the nonlinear model) in order to obtain the computer instructions corresponding to the discrete adjoint model.

In Appendix B we present the implementation of the adjoint method to compute the gradient of the cost functional. The adjoint model is the transpose of the tangent linear model (which is the linearized version of the nonlinear model). We discuss in Appendix B the coding strategy for both the adjoint and the tangent linear model and the necessary verifications for the correctness of the gradient computed using this method.

For research related to the description of the adjoint method and its implementation see Navon *et al.* [57, 58] and Yang and Navon [59].

5. NUMERICAL RESULTS

5.1. The optimization process

The optimization was performed over a short time interval (time window). The flow was computed over this time window and the values of the state variables for each time step in this control window were used in the adjoint computation (specifically the 'forcing term' for the adjoint equation).

The time window was located at the beginning of the time evolution and had a length varying between 1.0 and 4.0 time units.

Even when the flow is considered over a time period of 25.0 time units (which exceeds by far the length of the control time window), the optimized values of the control parameters suppress the Karman vortex shedding far beyond the extent of the time window.

The choice of the length of the time window is very important. For both cases, namely constant and time-dependent angular rotation, the length of the control window should be larger than the vortex shedding period (VSP), which is the inverse of the Strouhal number (the Strouhal number is defined by $St = \frac{f_K D}{U_0}$, where f_K is the Karman vortex street frequency and D is the diameter of the cylinder).

The adjoint method requires availability of the state variables' values for all the time steps in the control time window. For this reason we do not want the time-window length to be much larger than VSP, since this will increase both the memory and the CPU time requirements for minimization.

For the case of the constant rotation we obtained satisfactory results with a control time window smaller than VSP (but not smaller than 1.0 time unit). In the time-dependent case the choice of a time window smaller than VSP leads to nonconvergence of the minimization process.

The cost functional which was minimized involved the L_2 norm of the difference between the computed velocity and a 'desired' velocity. Our 'desired' flow was obtained for Reynolds number $Re = 2$ and the ratio between the angular velocity and the free stream velocity had a value of 2.0 (see Figure 2).

5.2. Suppression of Karman vortex shedding in the constant rotation case

We consider the speed ratio

$$\alpha = \frac{a\Omega}{U}$$

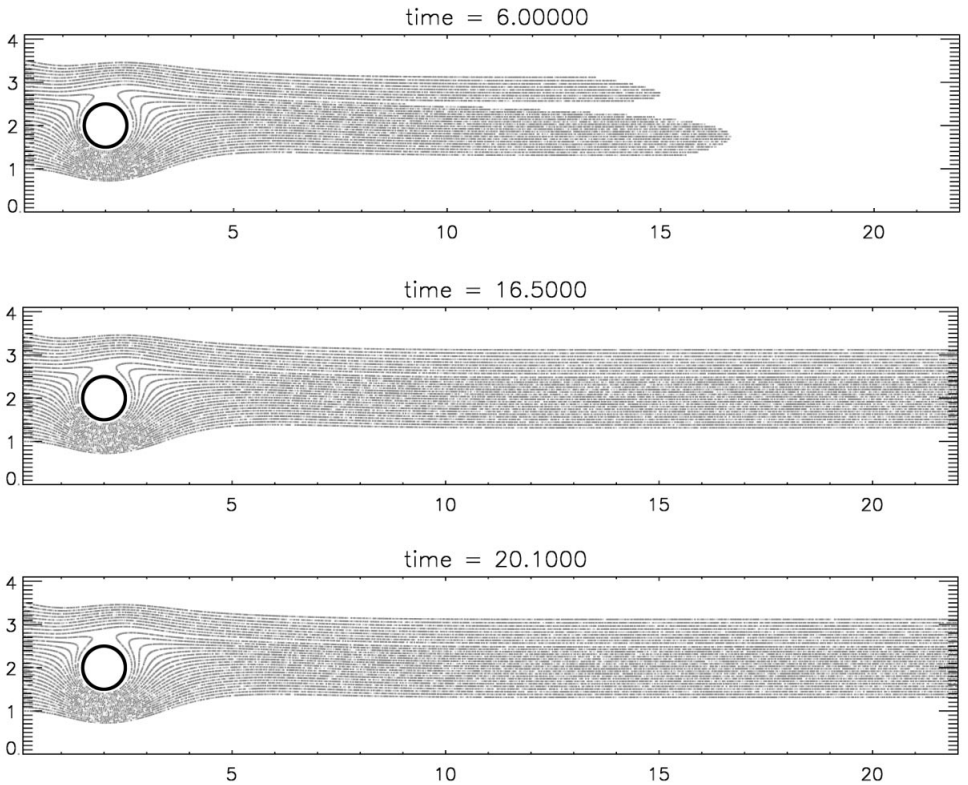

Figure 2. Streaklines for the 'desired' flow at $Re = 2$ and speed ratio $\alpha = 2.0$.

where a is the radius of the cylinder, Ω is the angular velocity and U is the free stream velocity.

The uncontrolled flow is taken at $\alpha = 0.5$ (an example is provided in Figure 1, for $Re = 100$). The minimization satisfies the convergence criteria after 5–11 minimization iterations for all the cases we considered: i.e. the Reynolds number taking the values $60 \leqslant Re \leqslant 1000$.

For each case considered we found a threshold value for α (denoted α_{Re}) such that for any $\alpha > \alpha_{Re}$ a full suppression of the Karman vortex shedding was obtained (see Figures 3, 4 and 5).

The CPU time required for a typical optimal flow control calculation was 2–3 h on a Silicon Graphics Indigo (SGI) machine.

The results for $60 \leqslant Re \leqslant 160$ were found to be in very good agreement with the numerical results obtained by Kang *et al.* [60] (see Figure 6).

For the case $60 \leqslant Re \leqslant 140$ the regularization parameter was found by using an empirically derived law relating it to the Reynolds number (see Figure 7). We started by finding the values of the regularization parameter by trial and error for two Reynolds numbers (we considered $Re = 60$ and $Re = 100$) and then we assumed the existence of a logarithmic relation between the regularization parameter and the Reynolds number. Based on this assumption

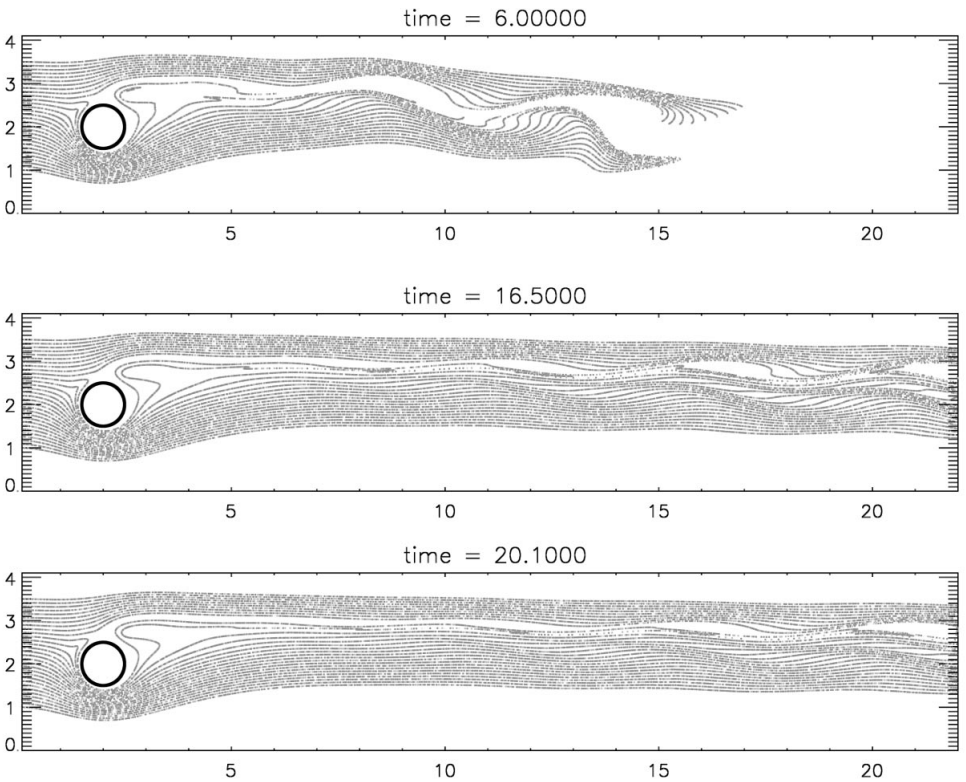

Figure 3. Streaklines for controlled flow at $Re = 100$ with optimal speed ratio $\alpha = 1.84$.

we were able to obtain the corresponding regularization parameters for the other Reynolds numbers (in our case $Re = 80$, $Re = 120$ and $Re = 140$, respectively).

For the case $160 \leqslant Re \leqslant 1000$ the empirical law employed in the previous case for obtaining the regularization parameter did not yield good results and, as a consequence, the corresponding regularization parameters were found by trial and error. A possible explanation of this phenomenon is the following: the Karman vortex regime for $160 \leqslant Re \leqslant 1000$ is inherently different than the regime for $60 \leqslant Re \leqslant 140$ (see Zdravkovich [61]).

To check that the minimization results were robust, we performed for each case two different minimizations: one starting with an initial guess of $\alpha = 0.9$ (a value less than the optimal value) and one starting with an initial guess of $\alpha = 3.5$ (a value greater than the optimal value of α). For both initial guesses, the results obtained for the optimal value of α were identical.

As the Reynolds number increases from 60 to 1000 we can see from Figure 8 that the rotation rate will tend asymptotically to a value which is in good agreement with previously obtained experimental and numerical results.

At $Re = 1000$ we compare our results with the values obtained by Chew *et al.* [62]. They found that for $\alpha = 2$ and $\alpha = 3$ any vortex shed will be weak and Karman vortex shedding almost disappears for $\alpha = 3$, a phenomenon which was also described experimentally by Badr *et al.* [3] and numerically by Chou [63]. We found the 'optimal' α to be $\alpha = 2.32$ for $Re = 1000$.

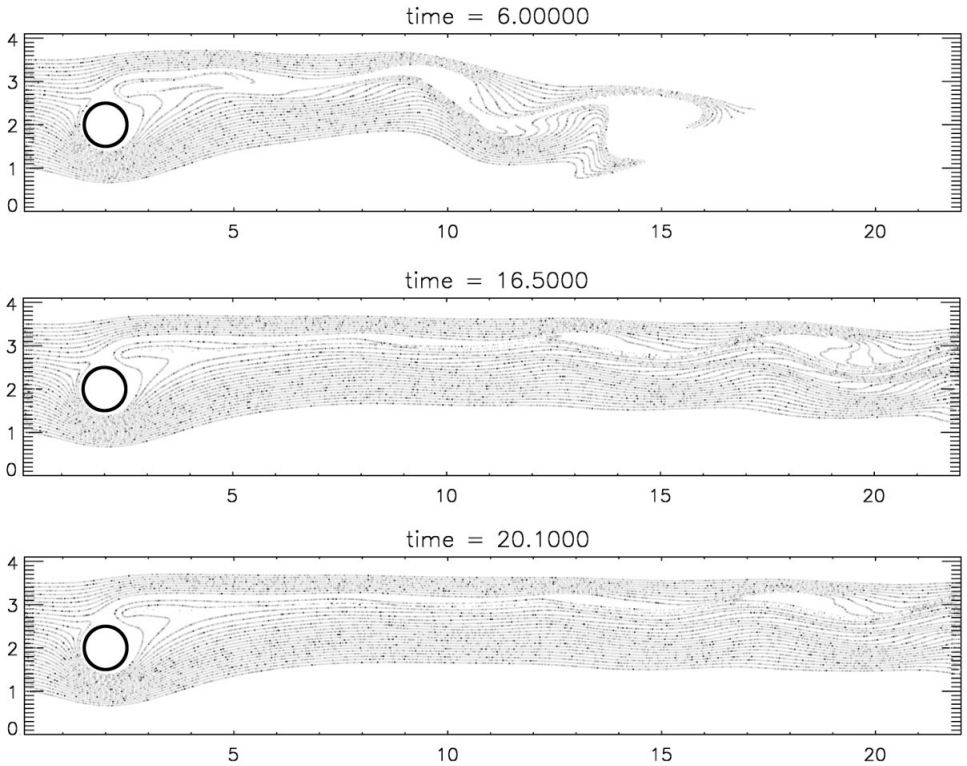

Figure 4. Streaklines for controlled flow at $Re = 400$ with optimal speed ratio $\alpha = 2.18$.

For $Re \geqslant 200$ the flow is not completely free of vortex shedding (as it can be seen from Figures 4 and 5). This situation was also described by Chen *et al.* [5].

In the case presented here (time independent angular velocity) we found that control time windows smaller than the Karman vortex shedding period (but not smaller than 1.0 time units) gave satisfactory results. This observation is important since a smaller control window reduces the computer memory necessary for storing of the state variables (which are required for the adjoint computation). A smaller time window also means a sizable reduction in the required CPU time.

5.3. The time histories of the drag coefficient in the constant rotation case

Practical applications (in aerodynamics) of optimal control for flow around a rotating cylinder involve the optimization of the drag coefficient (C_D).

We compare the variation of the drag coefficient in the controlled case (with rotation) with the corresponding variation for the no-rotation case ($\alpha = 0$). In order to compare them on the same plot we subtracted from C_D the corresponding mean value ($\bar{C}_D$). The mean drag coefficients obtained numerically for the case of no rotation were in agreement with the values reported by He *et al.* [26] (see Table I).

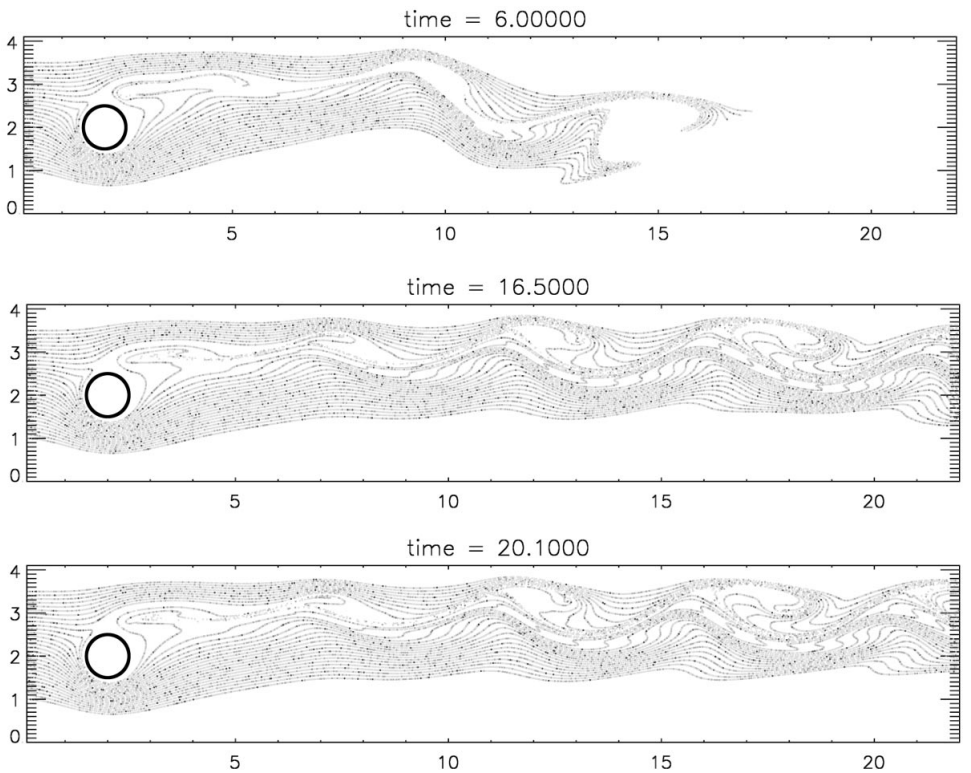

Figure 5. Streaklines for controlled flow at $Re = 1000$ with optimal speed ratio $\alpha = 2.35$.

We noticed a very significant reduction in the amplitude of the fluctuation for the drag coefficient when the flow is controlled.

In a viscous flow the total drag forces are contributed by the pressure and skin friction due to the viscous effects. For known vorticity values $(\omega(x, y) = [(\partial u/\partial y) - (\partial v/\partial x)])$ on the cylinder surface, the drag can be calculated in the polar coordinates $r - \theta$:

$$C_D(t) = C_{D_P}(t) + C_{D_f}(t) = \frac{2}{Re}\int_0^{2\pi}\left[\left(\frac{\partial\omega(t)}{\partial r}\right)\right]_\Gamma \sin\theta\,\mathrm{d}\theta - \frac{2}{Re}\int_0^{2\pi}[\omega(t)]_\Gamma \sin\theta\,\mathrm{d}\theta \qquad (12)$$

where the subscript Γ denotes quantities evaluated on the cylinder surface and the subscripts P and f represent the contributions from pressure and friction, respectively.

Figures 9 and 10 show plots of the time histories of the drag coefficient for different Reynolds numbers and for time in the interval $0 \leqslant t \leqslant 20$ time units. On each plot we present two graphs: the drag obtained for a flow in the fixed cylinder case ($\alpha = 0$) and, respectively, the drag for the flow obtained using the optimal value of the control speed ratio α (in each case we subtracted the corresponding mean value).

The results presented demonstrate the effectiveness in improving the drag performance by selecting a proper rotation rate, the Figures 9 and 10 showing a reduction of more than 60 per cent of the amplitude of the drag variation.

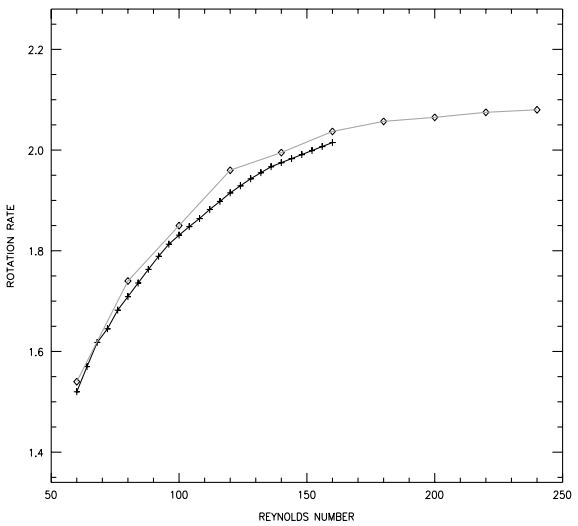

Figure 6. Comparison between our results ($\diamond$) and the results obtained by Kang *et al.* [60]: the speed ratio α vs. the Reynolds number.

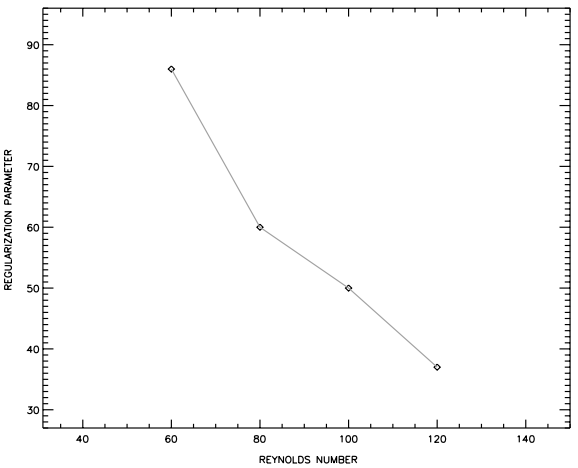

Figure 7. Regularization parameter vs. Reynolds number.

5.4. Suppression of Karman vortex shedding for the time harmonic rotary oscillation

Now we consider the angular velocity to be time-dependent. A special case is the time harmonic rotary oscillation, for which the speed ratio assumes the form $\alpha(t) = A\sin(2\pi Ft)$.

The minimization was performed for values of the Reynolds numbers in the range $100 \leqslant Re \leqslant 1000$.

Several time windows were used (the length of the control windows varying between 1.0 and 5.0 time units). In order to obtain numerical convergence for the minimization we had

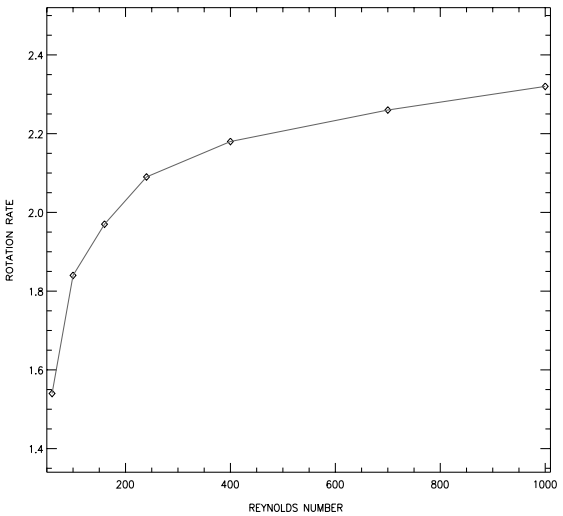

Figure 8. The optimal speed ratio α vs. the Reynolds number.

Table I. The mean value of the drag coefficient $\bar{C}_D$ for various Reynolds numbers.

Re	100	200	400	700	1000
Present work	1.42	1.44	1.54	1.59	1.68
He *et al.* [26]	1.35	1.36	1.42	1.48	1.52

to choose a time window longer than the Karman vortex shedding period, otherwise the minimization failed to converge.

The regularization parameter was chosen by trial and error. For this case we could not find a relationship between the regularization parameter and the Reynolds number, as for the previous constant rotation rate case.

The flow obtained using the optimal values of the angular velocity after the minimization is presented in Figures 11 and 12. In this case we do not obtain complete suppression of the vortex shedding. However, if we compare this flow with the uncontrolled flow (described in Figure 13) we can see that the flow is markedly less turbulent when the optimal rotation parameters provided by the minimization are employed.

5.5. The time histories of the drag coefficient for the time harmonic rotary oscillation

Reduction of the drag coefficient using time harmonic rotary oscillation was reported by Tokumaru and Dimotakis [4], Baek and Sung [6] and He *et al.* [26]. The research of He *et al.* [26] shows a 30 to 60 per cent drag reduction if one uses a rotating cylinder, compared to the fixed cylinder configuration.

Our results are presented in Figures 14 and 15 which show plots of the time histories of the drag coefficient for time in the interval $0 \leqslant t \leqslant 20$ time units.

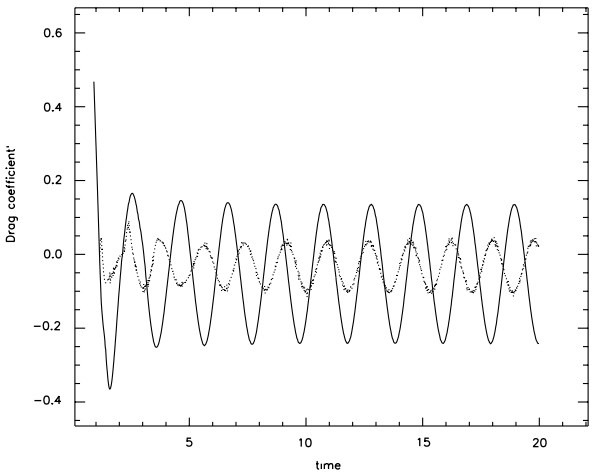

Figure 9. The variation of the drag in the controlled (dotted line) and uncontrolled case (continuous line) for $Re = 100$.

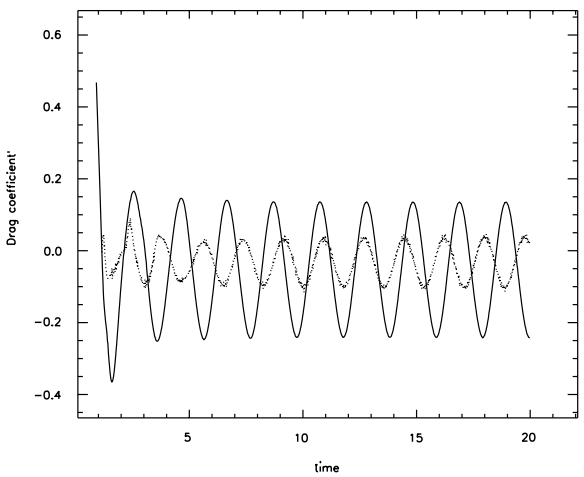

Figure 10. The variation of the drag in the controlled (dotted line) and uncontrolled case (continuous line) for $Re = 1000$.

They are not as impressive as the results obtained for the constant rotation case, a possible reason being that we could not obtain the full suppression of Karman vortex shedding.

Comparing our results with He *et al.* [26] we can distinguish small differences in the numerical values obtained for the optimal control parameters (in both research articles, the forcing angular velocity is $\omega(t) = \omega_1 \sin(2\pi S_e t)$ and the optimal control parameters are the amplitude ω_1 and the forcing frequency S_e). Our 'optimal' amplitude ω_1 differs by at most 10 per cent from the value reported in their research. We did not obtain the same 'optimal' forcing frequency (which in their case was very close to the lock-in forcing frequency).

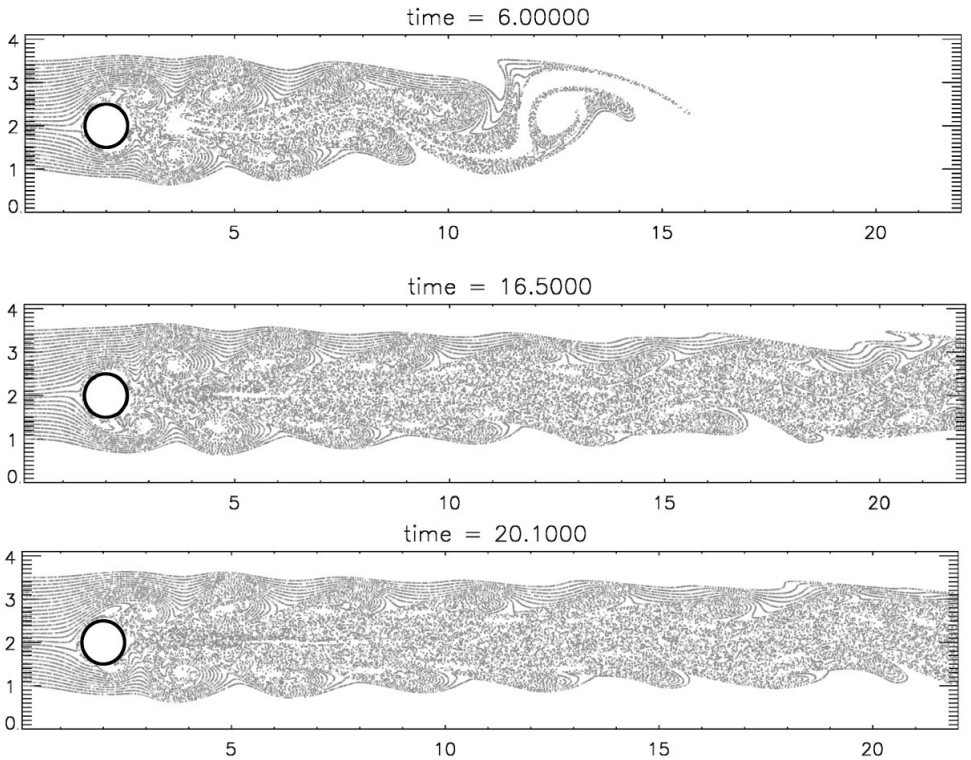

Figure 11. Streaklines for the controlled flow at $Re = 100$ with optimal parameters $A = 6.5,\ F = 1.13\ (\alpha(t) = A\sin(2\pi Ft))$.

One possible explanation for this situation is the following: there is a difference in the formulation of the cost functionals used in our research and those described in He *et al.* [26] (this difference appears to be due to the setting of the optimal control problem: our main goal was the suppression of the Karman vortex shedding, while their research aimed toward reduction of drag).

5.6. Description of the physical phenomena and their corresponding computational results

At low Reynolds numbers ($Re < 40$) the wake behind a non rotating cylinder comprises a steady recirculation region with two vortices symmetrically attached to the cylinder, whose size grows with increasing Reynolds number. When the Reynolds number is slightly larger, $Re < 60$, the trailing vortex street becomes unstable and develops an unsteady wavy pattern. For Reynolds numbers $60 < Re < 200$, the Karman vortex shedding occurs in the near wake behind a cylinder due to the flow instability accompanying a large fluctuating pressure and, thus, a periodically oscillating lift force. The attached vortices become asymmetric and are shed alternately at a well-defined frequency. At higher Reynolds numbers (i.e. $Re > 200$) the flow becomes more turbulent and vortex shedding also occurs, but assuming more complicated patterns this time. In this last case the vortex structures are unstable to 3-D

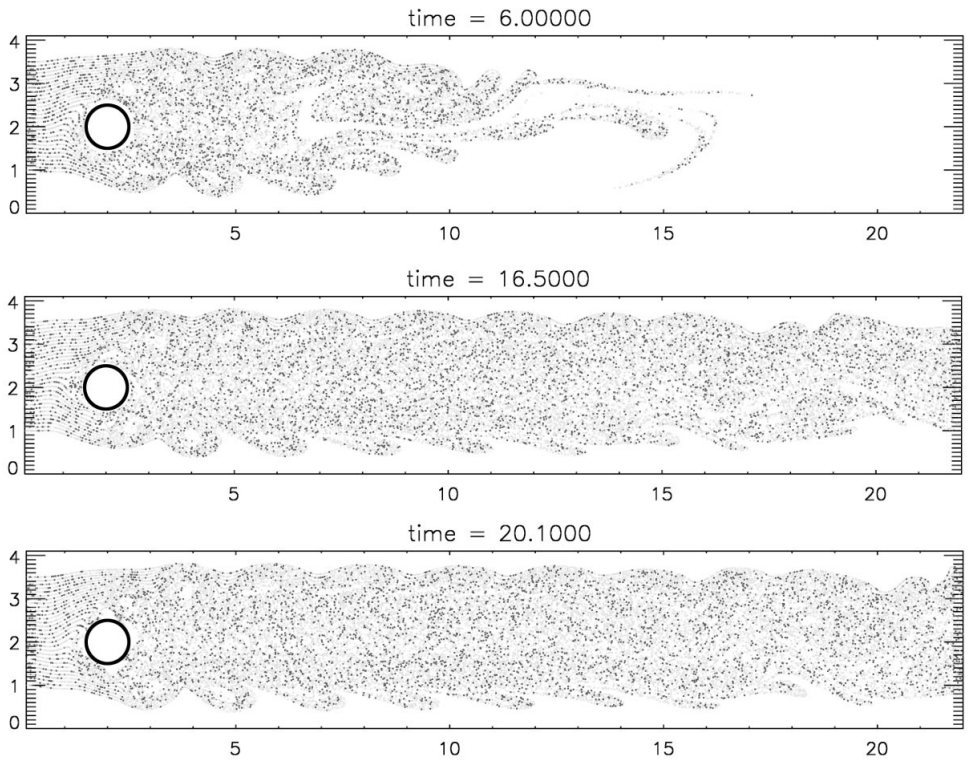

Figure 12. Streaklines for the controlled flow at $Re = 1000$ with optimal parameters $A = 6.0,\ F = 0.86\ (\alpha(t) = A\sin(2\pi Ft))$.

perturbations. For this reason, numerical results available from the 2-D codes agree well with the experimental data for Reynolds numbers $Re \leqslant 160$ but results obtained for larger Reynolds numbers are not always consistent as a consequence of the three-dimensionality effect (e.g. Graham [64]).

For higher Reynolds numbers 3-D codes will yield results which will match experimental data better than their 2-D counterparts. Zhang and Dalton [65] obtain smaller global quantities such as drag and lift (with better agreement with experimental values) than the corresponding 2-D simulation, the difference being attributed to the phase difference of flows in different spanwise locations caused by three-dimensionality and the 3-D mixing, both absent in the 2-D simulation.

For Reynolds numbers ($Re \geqslant 160$) there are various instabilities. After the wake undergoes a supercritical Hopf bifurcation (the primary instability) that leads to 2-D Karman vortex street the secondary instability occurs sequentially, which results in the onset of the 3-D flow. The periodic wakes are characterized by two critical modes which are respectively associated with large-scale and fine-scale structures in span (see Williamson [66], Ding and Kawahara [67]).

The rotation of a cylinder in a viscous uniform flow is expected to modify the wake flow pattern and vortex shedding configuration, which may reduce the flow-induced oscillation or

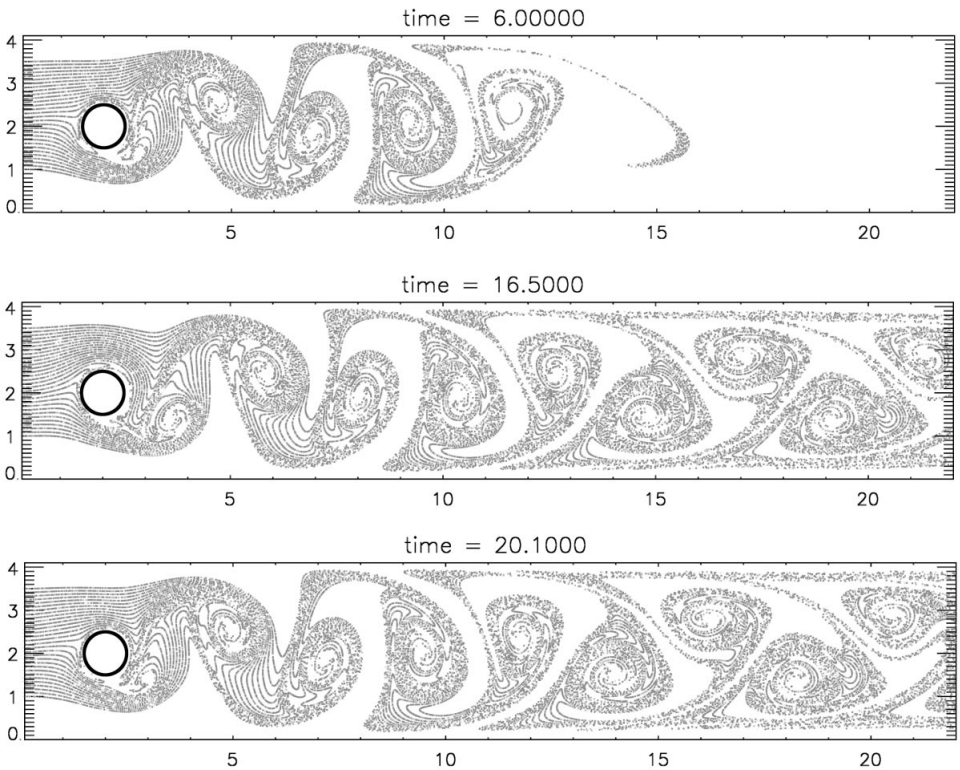

Figure 13. Streaklines for the uncontrolled flow at $Re = 100$ and speed ratio $\alpha(t) = 2.5\sin(1.0\pi t)$.

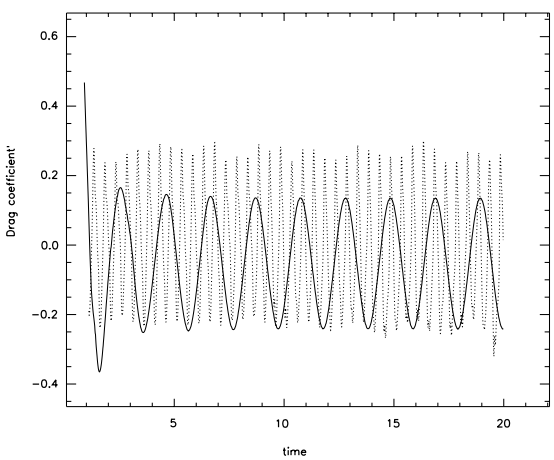

Figure 14. The variation of the drag in the controlled (dotted line) and uncontrolled case (continuous line) at $Re = 100$ for the time-dependent speed ratio $\alpha(t)$.

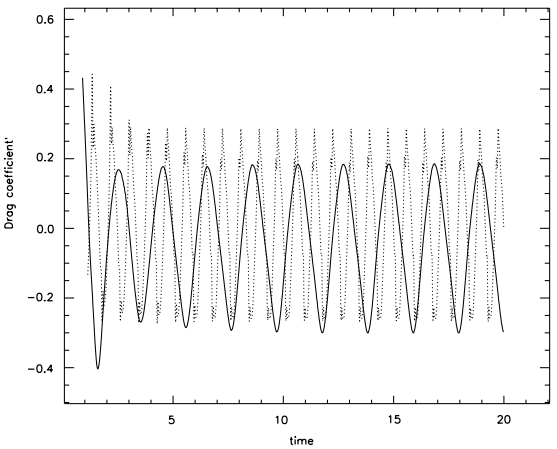

Figure 15. The variation of the drag in the controlled (dotted line) and uncontrolled case continuous line) at $Re = 1000$ for the time-dependent speed ratio $\alpha(t)$.

augment the lift force. The basic physical rationale behind the rotation effect is that as the cylinder rotates, the flow of the upper cylinder is decelerated and easily separated, while the flow of the lower cylinder is accelerated and the separation can be delayed or suppressed. Hence the pressure on the accelerated side becomes smaller than that of the decelerated side, resulting in a mean lift force (this effect is known as 'Magnus effect' (e.g. Reference [68])).

As we increase the control parameter α (the angular velocity normalized by the free stream velocity), the flow becomes asymmetric and at the same time the pressure on the lower (accelerated) side of the cylinder decreases, resulting in a negative downward mean lift. The rotation effect is mainly confined to the flow in the vicinity of the cylinder surface. For the near-surface flow, with increasing α the negative vorticity on the upper side of the cylinder dominates the positive vorticity on the lower side, thus weakening the vortex shedding which will eventually disappear.

There is a transition state (called *critical* state) between the state of periodically alternate double side shed vortex pattern for smaller α and the state of steady single side attached vortex pattern for larger α (e.g Ling and Shih [69], Badr *et al.* [3], Chen *et al.* [5]).

Another characteristic of the flow is the synchronization of cylinder and wake. This will determine the apparition of a 'lock-on' phenomenon. In the case of time harmonic rotary oscillations it was described experimentally by Tokumaru and Dimotakis [4] and numerically by Chou [9] and Dennis *et al.* [7] who studied the effects of the forcing frequency and amplitude on a cylinder wake. If the forcing frequency lies in the neighborhood of the natural Karman frequency the combined system of cylinder and wake will be locked in (and, according to He *et al.* [26], this is the optimal value for the forcing frequency for the drag reduction).

For this case (time dependent rotational oscillation) two co-rotating vortex pairs are shed away from the cylinder to form a co-rotating vortex pair which slows down their convection further downstream, which seems to delay the development of the periodic flow pattern in the near wake.

When the forcing frequency is lower than the natural shedding frequency an initial clockwise vortex is formed on the lower half of the cylinder when the cylinder is rotated in the counterclockwise direction and a counterclockwise vortex is formed on the upper half when the clockwise rotation starts. This leads to a non-synchronized vortex formation mode which cannot lead to suppression of Karman vortex shedding.

When the forcing frequency is higher than the natural shedding frequency an initial reactive clockwise vortex is formed on the upper half of the cylinder when the cylinder is rotated in the counterclockwise direction and a counterclockwise vortex is formed on the lower half when the clockwise rotation starts, which leads to a synchronized vortex mode (this is one of the reasons why the optimal values for the forcing frequency obtained in the previous section cannot be lower than the vortex shedding frequency).

The behavior of the drag coefficient C_D is determined by the fact that flow separation is a major source of pressure drag and the moving-wall effects will postpone this separation. As shown by Prandtl in 1925 [70] separation is completely eliminated on the side of the cylinder where the wall and the freestream move in the same direction and on the other side of the cylinder separation is developed only incompletely.

6. SUMMARY AND CONCLUSIONS

Suppression of Karman vortex shedding is achieved for a flow around a rotating cylinder using full optimal control. The numerical results obtained here agree to a large extent to results obtained by other researchers using other numerical or experimental methods to solve this problem.

An additional result obtained was the significant reduction of the amplitude of the drag coefficient using the rotation parameters given by the optimal control.

The main advantage of the optimal-control approach to flow control is the considerable freedom in choosing the objective function and the parameters of interest. However, this approach is very complex and quite demanding computationally.

The adjoint method for computing the gradient of the cost functional with respect to the control parameters provides us with the necessary tool to apply full optimal control to the problem of a flow around a rotating cylinder.

Our results were obtained for Reynolds numbers in the range $[60, 1000]$. The next step in our research will be to apply this method for higher Reynolds numbers.

Also a future research work related to this subject is to consider the application of the adjoint method to adaptive grids and exploiting the parallelism of this method. These issues are important factors in reducing the memory requirements (the adaptive grid) and improving the CPU time (both the adaptive grid and the parallelization).

This optimization problem is characterized by its ill-posedness. Our approach for circumventing it was the inclusion of a regularization term in the objective functional. An empirical law for finding suitable penalty parameters was found, allowing efficient minimization to be performed. There are other approaches for dealing with ill-posedness which can be used as well: the utilization of a second-order Tikhonov regularization function (e.g. Alekseev and Navon [71]) or the method of Singular Value Decomposition (SVD) which will decompose the problem into well-posed and ill-posed components (e.g. Liu *et al.* [72]).

ACKNOWLEDGEMENTS

The authors acknowledge the support from the School of Computational Science and Information Technology, Florida State University. They would like to thank Dr M. Y. Hussaini for his insightful comments. The second and third author acknowledge the support from the NSF grant number ATM-9731472 managed by Dr Pamela Stephens whom they would like to thank for her support.

7. APPENDIX A: DERIVING THE ADJOINT METHOD

In this section we present the adjoint method for the computation of the gradient of the cost functional with respect to the control parameters.

The cost functional has the following form:

$$\mathbf{J}[X,\Lambda]=\frac{1}{2}\sum_{k=0}^{R}[\mathbf{X}(t_k)-\mathbf{X}^{\mathrm{obs}}(t_k)]^T\mathbf{W}(t_k)[\mathbf{X}(t_k)-\mathbf{X}^{\mathrm{obs}}(t_k)] \tag{A1}$$

where $\mathbf{W}(t_k)$ is a diagonal weighting matrix, $t_0\leqslant t_k\leqslant t_R$, $[t_0,t_R]$ is the minimization window and R is the number of time steps in the minimization window.

To find the minimum of the cost functional, efficient minimization algorithms require the calculation of the gradient of the cost functional with respect to the control parameters: $(\nabla_\Lambda\mathbf{J}[\Lambda])^T$.

Near $\mathbf{X}(\tau)$ (the state vector at time τ) the nonlinear model can be written as:

$$\mathbf{X}(\tau+\Delta t)=\mathbf{F}(\mathbf{X}(\tau))$$

To calculate the gradient of the cost functional with respect to the control parameters we define the change in the cost function resulting from a small perturbation $\delta\mathbf{\Lambda}$ about the model control parameters $\mathbf{\Lambda}$:

$$\delta\mathbf{J}[X,\Lambda]=\mathbf{J}[X,\Lambda+\delta\mathbf{\Lambda}]-\mathbf{J}[X,\Lambda] \tag{A2}$$

As we take the limit $||\delta\mathbf{\Lambda}||\to 0$, $\delta\mathbf{J}[X,\Lambda]$ is the directional derivative in the $\delta\mathbf{\Lambda}$ direction and it is given by:

$$\delta\mathbf{J}[X,\Lambda]=\{\nabla_\Lambda\mathbf{J}[\Lambda]\}^T\delta\mathbf{\Lambda} \tag{A3}$$

On the other hand, $\delta\mathbf{J}[X,\Lambda]$ may also be expressed in the following form (using definition (A1) of the cost functional):

$$\delta\mathbf{J}[X,\Lambda]=\sum_{k=0}^{R}(\mathbf{W}(t_k)[\mathbf{X}(t_k)-\mathbf{X}^{\mathrm{obs}}(t_k)])^T\delta\mathbf{X}(t_k) \tag{A4}$$

where $\delta\mathbf{X}(t_k)$ is the perturbation of the state vector obtained from the perturbation of the model parameters $\delta\mathbf{\Lambda}$.

Combining relations (A3) and (A4) we obtain:

$$\{\nabla_\Lambda\mathbf{J}[X,\Lambda]\}^T\delta\mathbf{\Lambda}=\sum_{k=0}^{R}(\mathbf{W}(t_k)[\mathbf{X}(t_k)-\mathbf{X}^{\mathrm{obs}}(t_k)])^T\delta\mathbf{X}(t_k) \tag{A5}$$

From the above relation it is clear that we should express $\delta\mathbf{X}(t_k)$ as a function of $\delta\mathbf{\Lambda}$ in order to obtain an expression for $\nabla_\Lambda\mathbf{J}[X,\Lambda]$.

We start by linearizing the model about the current model solution:

$$\delta \mathbf{X}(t_0 + \Delta t) = \frac{\partial \mathbf{F}(X)(t_0)}{\partial \Lambda}\, \delta \mathbf{\Lambda} \tag{A6}$$

Using Equation (A6) for each time step we obtain:

$$\begin{aligned}
\delta \mathbf{X}(t_k) &= \mathbf{N}(t_k - \Delta t)\delta \mathbf{X}(t_k - \Delta t) \\
&= \mathbf{N}(t_k - \Delta t)\mathbf{N}(t_k - 2\Delta t)\delta \mathbf{X}(t_k - 2\Delta t) \\
&= \mathbf{N}(t_k - \Delta t)\mathbf{N}(t_k - 2\Delta t)\mathbf{N}(t_k - 3\Delta t)\delta \mathbf{X}(t_k - 3\Delta t) \\
&= \cdots \\
&= \mathbf{Q}_k \delta \Lambda
\end{aligned} \tag{A7}$$

where $\mathbf{N}(t) \equiv \partial \mathbf{F}[X(t)]/\partial \Lambda$ and $\mathbf{Q}_k$ represents the result of applying all the operator matrices in the linear model to obtain $\delta \mathbf{X}(t_k)$ from $\delta \Lambda$.

With the relation $\delta \mathbf{X}(t_k) = \mathbf{Q}_k \delta \Lambda$, equation (A5) becomes:

$$\nabla_\Lambda \mathbf{J}[X, \Lambda] = \sum_{k=0}^{R} \mathbf{Q}_k^T \mathbf{W}(t_k)[\mathbf{X}(t_k) - \mathbf{X}^{\text{obs}}(t_k)] \tag{A8}$$

We define the adjoint equations for the adjoint variables $\hat{\mathbf{\Lambda}}^{(k)}$:

$$\hat{\mathbf{\Lambda}}^{(k)}(t_0) = \mathbf{Q}_k^T \hat{\mathbf{\Lambda}}^{(k)}(t_k), \quad \text{for } k = 1, \ldots, R \tag{A9}$$

If the adjoint variable $\hat{\mathbf{\Lambda}}^{(k)}(t)$ at time t_k is initialized as:

$$\hat{\mathbf{\Lambda}}^{(k)}(t_k) = \mathbf{W}(t_k)[\mathbf{X}(t_k) - \mathbf{X}^{\text{obs}}(t_k)]$$

then the gradient of the cost function with respect to the control parameters is:

$$\nabla_\Lambda \mathbf{J}[X] = \sum_{k=0}^{R} \hat{\mathbf{\Lambda}}^{(k)}(t_k)$$

8. APPENDIX B: NUMERICAL IMPLEMENTATION OF THE ADJOINT METHOD

8.1. Coding the adjoint and the tangent linear method

If we linearize the nonlinear model we obtain the tangent linear model (TLM). The transpose of the TLM is the adjoint model.

For coding the TLM, we linearize the original nonlinear forward model code line by line, DO-loop by DO-loop and subroutine by subroutine.

If we view the tangent linear model as the result of the multiplication of a number of operator matrices: $\mathbf{A}_1 \mathbf{A}_2 \cdots \mathbf{A}_M$ where each matrix A_i, $i = 1, \ldots, M$ represents either a subroutine or a single DO-loop, then the adjoint model can be viewed as being a product of adjoint subproblems: $\mathbf{A}_M^T \mathbf{A}_{M-1}^T \cdots \mathbf{A}_1^T$.

The correctness of the adjoint of each operator was checked using the following identity:

$$(\mathbf{AQ})^T(\mathbf{AQ}) = \mathbf{Q}^T(\mathbf{A}^T(\mathbf{AQ}))$$

where **Q** represents the input of the original code and **A** can be either a single DO-loop or a subroutine. All subroutines of the adjoint model were subjected to this test.

The accuracy of the gradients calculated by the adjoint method should be at the level of machine precision. Errors could result due to coding mistakes, round-off errors or the presence of non differentiable functions.

A method for the gradient check is described below, using the following Taylor expansion of the cost functional:

$$\mathbf{J}(X + \eta h) = \mathbf{J}(\mathbf{X}) + \eta \mathbf{h}^T \nabla \mathbf{J}(X) + O(\eta^2) \tag{A10}$$

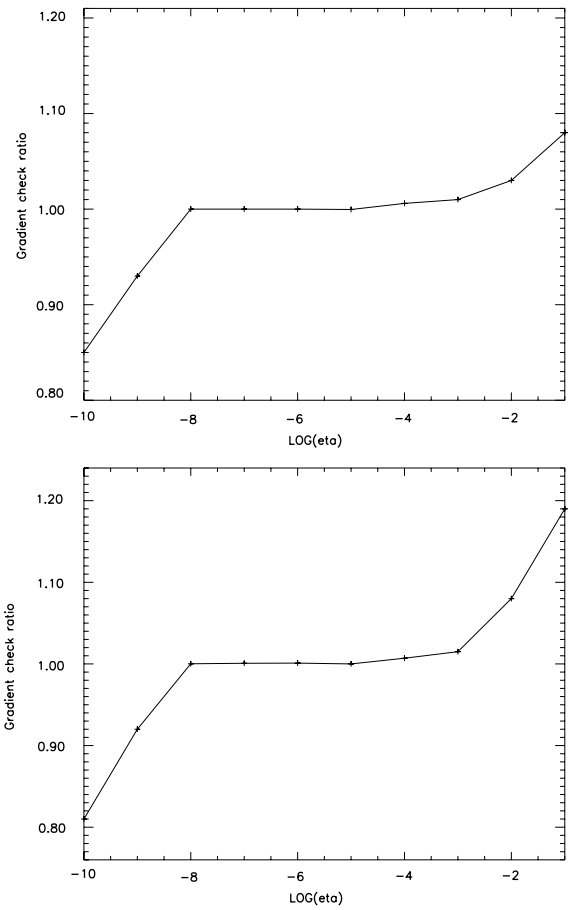

Figure A1. The accuracy check for the gradient for the constant rotation case (top) and time-dependent rotation case (bottom).

where $||\mathbf{h}|| = 1$, η scalar and $\nabla \mathbf{J}(\mathbf{X})$ is the gradient of the cost functional $\mathbf{J}(\mathbf{X})$ with respect to $\mathbf{X}$ computed using the adjoint code.

Rewriting the above formula, a function of η can be defined as (see Navon *et al.* [57]):

$$\mathbf{\Phi}(\eta) = \frac{\mathbf{J}(\mathbf{X} + \eta\mathbf{h}) - \mathbf{J}(\mathbf{X})}{\eta \mathbf{h}^{\mathbf{T}} \nabla \mathbf{J}(\mathbf{X})} \tag{A11}$$

The gradient computed using the adjoint model can be assumed to be completely accurate (up to the machine error) when $\lim_{\eta \to 0} |\mathbf{\Phi}(\eta)| = 1$. A validity region of the gradient test is normally obtained for $10^{-3} \geqslant \eta \geqslant \varepsilon$ (where ε is the machine accuracy). For $\eta > 10^{-3}$ we have truncation error and for η near the machine accuracy roundoff errors prevail.

The results of the gradient check test are displayed in Figure A1.

REFERENCES

1. von Karman T. Uber den Mechanismus des Widerstandes, den ein bewegter Korper in einer Flussigkeit erzeugt. *Nachr. Ges. Wiss. Gottingen*, *Math. Phys. Klasse* 1911; 509–517.
2. Badr H, Coutanceau M, Dennis S, Menard C. Sur la comparaison des calculs numeriques et des visualisations de l'ecoulement d'un fluide visqueux engendre par un cylindre en translation et rotation. *Comptes Rendus de L'Academie des Sciences Paris* 1985; **300**(12):529–533.
3. Badr H, Coutanceau M, Dennis S, Menard C. Unsteady flow past a rotating circular cylinder at Reynolds numbers 1000 and 10000. *Journal of Fluid Mechanics* 1990; **220**:459–484.
4. Tokumaru T, Dimotakis P. Rotary oscillation control of a cylinder wake. *Journal of Fluid Mechanics* 1991; **224**:77–90.
5. Chen Y, Ou Y-R, Pearlstein A. Development of the wake behind a circular cylinder impulsively started into rotatory and rectilinear motion. *Journal of Fluid Mechanics* 1993; **253**:449–484.
6. Baek S, Sung H. Numerical simulation of the flow behind a rotary oscillating circular cylinder. *Physics of Fluids* 1998; **10**(4):869–876.
7. Dennis S, Nguyen P, Rocabiyik S. The flow induced by a rotationally oscillating and translating circular cylinder. *Journal of Fluid Mechanics* 2000; **407**:123–144.
8. Juarez H, Scott R, Metcalfe R, Bagheri B. Direct simulation of freely rotating cylinders in viscous flows by high-order finite element methods. *Computers and Fluids* 2000; **29**:547–582.
9. Chou MH. Synchronization of vortex shedding from a cylinder under rotary oscillation. *Computers and Fluids* 1997; **26**(8):755–774.
10. Gad-El-Hak M. Modern developments in flow control. *Applied Mechanics Reviews* 1996; **49**:365–379.
11. Gad-El-Hak M. *Flow control*: *Passive*, *active and reactive flow management*. Cambridge University Press: Cambridge, U.K., 2000; 421.
12. Modi VJ. Moving surface boundary-layer control: A review. *Journal of Fluids and Structures* 1997; **11**(6): 627–663.
13. Tang S, Aubry N. Suppression of vortex shedding inspired by a low dimensional model. *Journal of Fluids and Structures* 2000; **14**:443–468.
14. Gillies E. Low dimensional control of the circular cylinder wake. *Journal of Fluid Mechanics* 1998; **371**: 157–178.
15. Gunzburger M, Lee H. Feedback control of Karman vortex shedding. *Transactions of ASME — Journal of Applied Mechanics* 1996; **63**:828–835.
16. Huang X. Feedback control of vortex shedding from a circular cylinder. *Experiments in Fluids* 1996; **20**: 218–224.
17. Joslin R, Gunzburger M, Nicolaides R, Erlebacher G, Hussaini MY. Self-contained automated methodology for optimal flow control. *AIAA Journal* 1997; **35**(5):816–824.
18. Kwon K, Choi H. Control of laminar vortex shedding behind a circular cylinder using splitter plates. *Physics of Fluids* 1996; **10**:479–485.
19. Ozono S. Flow control of vortex shedding by a short splitter plate asymmetrically arranged downstream of a cylinder. *Physics of Fluids* 1999; **11**(10):2928–2934.
20. You D, Choi H, Choi M, Kang S. Control of flow-induced noise behind a circular cylinder using splitter plates. *AIAA Journal* 1998; **36**(11):1961–1967.
21. Park D, Ladd D, Hendricks E. Feedback control of von Karman vortex shedding behind circular cylinders at low Reynolds numbers. *Physics of Fluids* 1994; **6**(7):2390–2405.

22. Sakamoto H, Haniu H. Optimum suppression of fluid forces acting on a circular cylinder. *Journal of Fluids Engineering* 1994; **116**:221–227.
23. Tang K, Graham W, Peraire J. Active flow control using a reduced order model and optimum control. *AIAA Paper* 1996; **96-1946**.
24. Tao JS, Huang XY, Chan WK. A flow visualization study of feedback control of vortex shedding from a circular cylinder. *Journal of Fluids and Structures* 1996; **10**:965–970.
25. Warui H, Fujisawa N. Feedback control of vortex shedding from a circular cylinder by cross flow cylinder oscillations. *Experiments in Fluids* 1996; **21**:49–56.
26. He JW, Glowinski R, Metcalfe R, Nordlander A, Periaux J. Active control and drag optimization for flow past a circular cylinder I: Oscillatory cylinder. *Journal of Computational Physics* 2000; **163**(1):83–117.
27. Tokumaru T, Dimotakis P. The lift of a cylinder executing rotary motions in a uniform flow. *Journal of Fluid Mechanics* 1993; **255**:1–10.
28. Pentek A, Kadtke J. Dynamical control for capturing vortices near bluff bodies. *Physical Review E* 1998; **58**(2):1883–1898.
29. Choi H, Hinze M, Kunisch K. Instantaneous control of backward-facing step flows. *Applied Numerical Mathematics* 1999; **13**:133–158.
30. Ito K, Ravindran SS. A reduced-order method for simulation and control of fluid flows. *Journal of Computational Physics* 1998; **143**(2):403–425.
31. Graham WR, Peraire J, Tang KY. Optimal control of vortex-shedding using low order models. Part I: Open-Loop Model development. *International Journal of Numerical Methods in Engineering* 1999; **7**:950–971.
32. Graham WR, Peraire J, Tang KY. Optimal control of vortex-shedding using low order models. Part II: Model Based Control. *International Journal of Numerical Methods in Engineering* 1999; **7**:972–990.
33. Afanasiev K, Hinze M. Adaptive control of a wake flow using proper orthogonal decomposition. *Technische Universitat Berlin* 1999; **648**/1999.
34. Abergel F, Temam R. On some control problems in fluid mechanics. *Theoretical and Computational Problems in Fluid Dynamics* 1990; **1**:303–325.
35. Gunzburger M, Hou L, Svobodny T. Boundary velocity control of incompressible flow with an application to viscous drag reduction. *SIAM Journal of Control and Optimization* 1992; **30**(1):167–181.
36. Hou L, Yan Y. Dynamics and approximations of a velocity tracking problem for the Navier–Stokes flows with piecewise distributed controls. *SIAM Journal on Control and Optimization* 1997; **35**(6):1847–1885.
37. Hou L, Ravindran SS, Yan Y. Numerical solutions of optimal distributed control problems for incompressible flows. *International Journal of Computational Fluid Dynamics* 1997; **8**:99–114.
38. Berggren P. Numerical solution of a flow control problem: vorticity reduction by dynamic boundary action. *Siam Journal in Control and Optimization* 1998; **19**(3):829–860.
39. Bewley T, Temam R, Ziane M. A general framework for robust control in fluid mechanics. *Physica D* 2000; **138**:360–392.
40. Ghattas O, Bark J. Optimal control of 2-D and 3-D incompressible Navier–Stokes flows. *Journal of Computational Physics* 1997; **136**:231–244.
41. Li Z, Navon IM, Hussaini YM, LeDimet FX. Optimal control of the unsteady Navier–Stokes equations. *Computers & Fluids* 2000; submitted for publication.
42. Gunzburger M, Manservisi S. The velocity tracking problem for Navier–Stokes flows with bounded distributed controls. *SIAM Journal of Control and Optimization* 1999; **37**(6):1913–1945.
43. Gunzburger M, Hou L, Svobodny T. Analysis and finite element approximation of optimal control problems for the stationary Navier–Stokes equations with distributed and Neumann controls. *Mathematics of Computation* 1991; **57**(195):123–151.
44. Hou L, Ravindran SS. Penalty methods for numerical approximations of optimal boundary flow control problems. *International Journal of Computational Fluid Dynamics* 1998; **11**:157–167.
45. Hou L, Ravindran SS. A penalized Neumann control approach for solving an optimal Dirichlet control problem for the Navier–Stokes equations. *Siam Journal of Control and Optimization* 1998; **36**(5):1795–1814.
46. Gunzburger M. Sensitivities, adjoints and flow optimization. *International Journal for Numerical Methods in Fluids* 1999; **31**:53–78.
47. Griebel M, Dornseifer T, Neunhoeffer T. Numerical simulation in fluid dynamics. *SIAM Monographs on Mathematical Modeling and Computation* 1998; **3**.
48. Burns JA, Ou Y-R. Effect of rotation rate on the forces of a rotating cylinder: simulation and control. *ICASE Report* 1993; **93-11**.
49. Ou Y-R. Mathematical modeling and numerical simulation in external flow control. In *Flow Control*, Gunzburger M (ed.). Springer-Verlag, 1996; 218–253.
50. Coron J. On the controllability of the 2-D incompressible Navier–Stokes equations with the Navier slip boundary equations. *ESAIM*: *Control*, *Optimization and Calculus of Variations* 1996; **1**:35–75.
51. Fursikov A, Gunzburger M, Hou L. Boundary value problems and optimal boundary control for the Navier–Stokes system: the two-dimensional case. *SIAM Journal of Control and Optimization* 1998; **36**(3):852–894.

52. Sritharan SS. An optimal control problem in exterior hydrodynamics. *Proceedings of the Royal Society of Edinburgh* 1992; **121A**:5–32.
53. Press WH, Teukolsky SA, Vetterling WT, Flannery BP. *Numerical Recipes in C. The Art of Scientific computing* (2nd edn). Cambridge University Press: Cambridge, U.K., 1997. http://www.ulib.org/webroot/Books/NumericalRecipes.
54. Tikhonov AN, Arsenin VY. *Solutions of Ill-posed Problems*. Winston, 1977.
55. Hansen PC. Rank-deficient and discrete ill-posed problems: numerical aspects of linear inversion. *SIAM Monographs on Mathematical Modelling and Computation* 1997; **4**.
56. Alifanov OM, Artiukhin EA, Rumyantsev SV. *Extreme Methods for Solving Ill-posed Problems with Applications to Inverse Heat Problems.* Begell House, 1995.
57. Navon IM, Zou X, Derber J, Sela J. Variational data assimilation with an adiabatic version of the NMC spectral model. *Monthly Weather Review* 1992; **120**:1433–1446.
58. Navon IM. Practical and theoretical aspects of adjoint parameter estimation and identifiability in meteorology and oceanography. *Dynamics of Atmospheres and Oceans* 1998; **27**(1–4):55–79.
59. Yang W, Navon IM. Documentation of the tangent linear model and its adjoint of the adiabatic version of the NASA GEOS-1 C-grid GCM. NASA Technical Memorandum 104606 March 1996; vol. 8, 61 pp. http://hera.gsfc.nasa.gov/subpages/tech-reports.html.
60. Kang S, Choi H, Lee S. Laminar flow past a rotating circular cylinder. *Physics of Fluids* 1999; **11**(11): 3312–3321.
61. Zdravkovich MM. *Flow Around Circular Cylinders*, vol. 1. Oxford University Press: Oxford, U.K., 1997.
62. Chew YT, Cheng M, Luo SC. A numerical study of flow past a rotating circular cylinder using a hybrid vortex scheme. *Journal of Fluid Mechanics* 1995; **299**:35–71.
63. Chou MH. Numerical study of vortex shedding from a rotating cylinder immersed in a uniform flow field. *International Journal for Numerical Methods in Fluids* 2000; **32**:545–567.
64. Graham JMR. Report on the session comparing computation of flow past circular cylinders with experimental data. In *Proceedings of IUTAM Symposium*: *Bluff-Body Wakes*, *Dynamics and Instabilities*, 7–11 September, 1992, Gottingen, Eckelmann H, Graham JMR, Huerre P, Monkewitz PA (eds). Springer Verlag, 1993.
65. Zhang J, Dalton C. A three-dimensional simulation of a steady approach flow past a circular cylinder at low Reynolds number. *International Journal for Numerical Methods in Fluids* 2000; **26**: 1003–1022.
66. Williamson CHK. Vortex dynamics in the cylinder wake. *Annual Review of Fluid Mechanics* 1996; **28**:477–539.
67. Ding Y, Kawahara M. Secondary instabilities of wakes of a circular cylinder using a finite element method. *International Journal of Computational Fluid Dynamics* 2000; **13**(3):279–312.
68. Barkla HM, Auchterlonie LJ. The Magnus or Robins effect on Rotating Spheres. *Journal of Fluid Mechanics* 1971; **47**(3):437–447.
69. Ling GP, Shih TM. Numerical study on the vortex motion patterns around a rotating circular cylinder and their critical characters. *International Journal for Numerical Methods in Fluids* 1999; **29**:229–248.
70. Prandtl L. Bericht ueber Untersuchungen zur ausgebileten Turbulenz. *ZAMM* 1925; **3**:136–139.
71. Alekseev A, Navon IM. The analysis of an ill-posed problem using multiscale resolution and second order adjoint techniques. *Computer Methods in Applied Mechanics and Engineering* 2001; **190**(15–17):1937–1953.
72. Liu J, Guerrier B, Benard C. A sensitivity decomposition for the regularized solution of the inverse heat conduction problems by wavelets. *Inverse Problems* 1995; **11**:1177–1187.

